Topics in Catalysis (2022) 65:1745–1754
https://doi.org/10.1007/s11244-022-01626-1

ORIGINAL PAPER

Degradation of Methylene Blue Dye and Bisphenol-A Using Expanded Graphene-Polypyrrole-Magnetite Nanocomposite

Onoyivwe Monday Ama[1] · Uyiosa Osagie Aigbe[2] · William Wilson Anku[3] · Otolorin Adelaja Osibote[2] · Kaushik Pal[4]

Accepted: 5 May 2022 / Published online: 30 May 2022

Abstract

This work is focused on the synthesis of expanded graphene (EG), polypyrrole-magnetite (PPy/Fe_3O_4) and expanded graphene-polypyrrole-magnetite nanocomposite (EG-PPy/Fe_3O_4) electrodes and their application in the degradation of organic pollutants in water. The nanocomposites were synthesized through the co-precipitation method and characterized using ultraviolet–visible spectroscopy, Brunauer–Emmett–Teller surface area analyser, scanning electron microscope, energy dispersive X-ray, X-ray diffractometer and X-ray photoelectron spectroscope. The EG, PPy/Fe_3O_4 and EG-PPy/Fe_3O_4 electrodes were applied in a comparative photoelectrochemical degradation of 0.1×10^{-4} M methylene blue (MB) dye and bisphenol A (BPA) in 0.1 M Na_2SO_4 under visible light irradiation. The degradation was also performed through photolysis, electrochemical and photoelectrochemical processes. The results showed that the pure PPy and EG-PPy/Fe_3O_4 were present in the Anatase phase of PPy. The EG-PPy/Fe_3O_4 composite absorbed a noticeable amount of light in the entire visible light region compared to pure PPy and PPy/Fe_3O_4. The surface area and pore volume of pure PPy was observed to decrease after modification with the EG as a result of the interpenetration of the porous matrix of EG by the PPy nanoparticles. The EG-PPy/Fe_3O_4 electrode was the most effective in the degradation of both dyes. The order of efficiency was EG < PPy/Fe_3O_4 < EG-PPy/Fe_3O_4. The photoelectrochemical degradation process resulted in improved degradation efficiency of 92% (MB) and 88% (BPA) within 240 min and was observed to be greater than that of photolysis and electrochemical oxidation methods. The EG-PPy/Fe_3O_4 photoanode is regarded as an effective material for the degradation of MB and BPA in wastewater.

Graphical Abstract

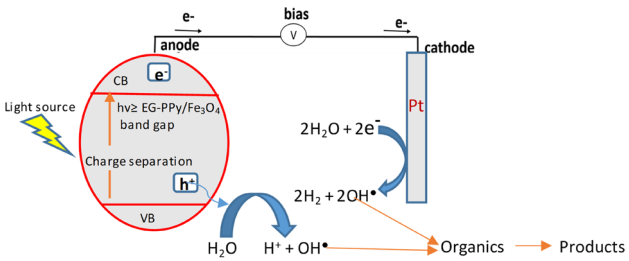

Keywords Photoelectrochemical degradation · Photoanode · Contaminants · Energy bandgap · Nanocomposite

✉ Uyiosa Osagie Aigbe
uyi4we@gmail.com

Onoyivwe Monday Ama
onoyivwe4real@gmail.com

[1] DST-CSIR National Center for Nanostructured Materials Council for Scientific and Industrial Research, Pretoria 0001, South Africa

[2] Department of Mathematics and Physics, Cape Peninsula University of Technology, Cape Town 8000, South Africa

[3] CSIR-Water Research Institute, P.O. Box M32, Accra, Ghana

[4] University Centre for Research and Development (UCRD), Department of Physics, Chandigarh University, Gharuan, Mohali, Punjab 140413, India

1 Introduction

In recent years, poor sanitation, waterborne contaminations, deterioration of water quality, and absence of clean water supply are of great concern, owing to the increase in human population and fast-growing industries [1, 2]. The profusion and distribution of plastic particles in the environment and the effect of organic compounds leaching from plastic debris have been of great concern lately [3]. Some of these compounds released into the environment through anthropogenic processes are classified as endocrine-disrupting chemicals (EDCs). EDCs are referred to as exogenous chemicals; as they can accumulate in biota and interfere with biological activities such as the inhibition of hormone receptors which can pose health hazards to humans and animals [4, 5].

BPA is a synthetic organic compound and a common industrial product, manufactured in huge quantities globally. It is an EDCs and is widely used in the chemical industry in the production of polycarbonate plastic as well as epoxy resin, which are practical materials present in food containers. Polycarbonate effluents have been found to contain high amounts of BPA (about 100 mg/L), which might result in severe health effects like human prostate cancer, cardiovascular diseases, diabetes mellitus, hormonal imbalance, liver and enzyme abnormalities, in addition to reproduction problems [6–9].

Another group of pollutants released into water bodies are dyes e.g., methylene blue dye (MB). The existence of these dyes in the environment is a problem of great concern. Most of them are toxic and hence pose a serious threat to both aquatic life and human well-being. Even at low concentrations, these dyes change the colour of the water bodies. This occurrence prevents light penetration of the water bodies which affects the photosynthetic processes in the water adversely, disturbing aquatic ecosystems [10]. Textile dyes are also toxic, mutagenic, and carcinogenic [11, 12]. They persist as environmental pollutants, cross entire food chains and undergo biomagnification [13], resulting in higher levels of contamination at higher trophic levels [14]. Industrial wastewater contaminated with toxic dyes must, therefore, be treated before its final release into the surroundings.

Several methods have been employed for the removal of these pollutants. These methods include the physical adsorption, chemical as well as biological degradation processes. Physical techniques were observed to transfer pollutants from one form to another without their complete eradication. For biological processes, a long treatment period was required and the application of these processes was limited to very low contaminant concentrations. The chemical treatment processes led to products with higher endocrine-disrupting effects (EDCs). Thus, most of these methods reported were found to be inefficient or gave rise to hazardous by-products, which resulted in secondary contamination [5, 15, 16].

A promising technique for the mineralization of highly stable organic contaminants such as surfactants, pesticides, phenolic wastes and colouring materials, and inorganic contaminants is the advanced oxidation process (AOP). Currently, in wastewater treatment for BPA and MB, AOPs which use semiconductor materials as a photocatalyst have widely been applied. The effectiveness of the photocatalyst is generally considered by its capacity to instantaneously adsorb reactants and photon energy, as this is shown by the photosensitivity of the catalyst and its bandgap [7, 17–20]. The in-situ generation of very reactive chemical species like hydroxyl radicals, which cause the non-specific mineralization of target contaminants with high reaction rates and negligible generation of secondary waste is the mechanism that makes AOPs effective. However, the shortcoming of these remediation procedures is that they are regularly expensive [21]. To enhance the rates of degradation and reduce the operational time, an improved AOP consisting of a combination of metal oxide nanoparticles and biopolymers has attracted huge attention [19].

Lately, magnetic nanocomposites have received great attention. They have been used broadly for environmental applications owing to their unique properties including ease of functionalization, large surface-to-volume ratio, environmentally friendly nature, effective separation owing to their magnetic properties and low cost. An approach for preparing magnetically recoverable catalysts is the control of the metal ions onto the magnetic nanoparticles by altering the metal ions' surface with organic molecules. This is done to protect the magnetic core against oxidation and particle aggregation [21]. In the current study, magnetite (core) was stabilized using eco-friendly polymer (polypyrrole) and expanded graphene to form an EG-PPy/Fe_3O_4 composite. The composite was developed into an electrode and used as a catalyst for improving the photodegradation of BPA and MB in synthetic wastewater.

2 Materials and Methods

2.1 Chemicals

All chemicals used were of analytical grade and used without further change. Pyrrole monomer (Py), BPA, magnetite (Fe_3O_4), ferric chloride ($FeCl_3$), sodium hydroxide (NaOH), and hydrochloric acid (HCl) were all purchased from Sigma Aldrich (South Africa).

2.2 Synthesis of Expanded Graphene

The synthesis of exfoliated graphite involved the addition of H_2SO_4/HNO_3 mixture in the ratio of 3:1 (300:100 mL) to 20 g of natural graphite after which the mixture was stirred vigorously with a magnetic starrier for 12 h. The resultant mixture was then washed abundantly with deionized water until a neutral pH was obtained. The residue was oven-dried at 100 °C for 24 h to obtain a graphite intercalated compound. The EG was finally obtained by heating the graphite intercalated compound at 800 °C for 1 min in a furnace.

2.3 Synthesis of PPy/Fe_3O_4 Nanocomposite

The in-situ oxidative polymerization procedure described by [22] was used for the synthesis of the polymer-based magnetic nanocomposite. 0.4 g of Fe_3O_4 (magnetite) was added to 80 mL of deionized water in a 250 mL Erlenmeyer flask. The suspension was ultrasonicated for 1 h for proper dispersion of the Fe_3O_4 in the deionized water. 0.8 mL of pyrrole was syringed into the suspension of the magnetite, with the subsequent addition of 6 g of oxidant ($FeCl_3$) to the nanoparticles suspended solution. The nanoparticle suspended solution was stirred manually for 15 min at room temperature to make a homogeneous mixture. The mixture was kept for 3 h for complete polymerization to take place. The black residue obtained was washed with distilled water. Acetone was subsequently added to the filtrate until it becomes colourless. The synthesized nanocomposite (PPy/Fe_3O4) was dried under a vacuum at 60 °C for 24 h.

2.4 Synthesis of EG-PPy/Fe_3O_4 Nanocomposite

The synthesised EG was dispersed into deionized water in a ratio of 1:1 the mixture was continuously stirred for 12 h and subjected to 6 h of sonication. The PPy/Fe_3O_4 (1 g) was mixed with the dispersed EG. The mixture was sonicated for another 4 h, and oven-dried for 6 h at 100 °C. The EG-PPy/Fe_3O_4 nanocomposites were pelleted and used to produce the electrode. The EG-PPy/Fe_3O_4 electrode was produced by following the procedure described in Sect. 2.6 below.

2.5 Characterization of EG-PPy/Fe_3O_4 Nanocomposite

The synthesized EG-PPy/Fe_3O_4 nanocomposite was characterized using X-ray diffraction (XRD) to determine its crystalline structure. The scanning electron microscopy (SEM) coupled with the energy dispersive X-ray spectrometry (EDX) was used to determine the surface morphology and elemental composition of the synthesized composite, while the various functional groups in the nanocomposite were determined using the Fourier transform infrared spectrometry (FTIR). To get detailed information about the surface area and cumulative pore volume of the EG-PPy/Fe_3O_4, a Brunauer–Emmett–Teller (BET) analysis was done. The optical properties were examined via UV–Vis absorbance and diffuse reflectance spectroscopy studies using dry powders with LAMBDA 750 as the internal standard.

2.6 EG-PPy/Fe_3O_4 Electrode Fabrication

The EG-PPy/Fe_3O_4 synthesized (150 mg) was compressed into a pellet with a diameter of 1 cm, which was subsequently cut out into small bits. A copper wire was coiled at one end of a glass tube with conducting silver paint causing the wire to form a flat surface at that end of the glass tube. The pellet pieces were then deposited on the flat copper wire surface and covered with epoxy resin. This was done to ensure that the current comes from only the basal plane to ensure effective electron transmission.

2.7 Photoelectrochemical Degradation

The Photoelectrochemical activity of the synthesized photoanodes was studied in a photo-reactor involving H_2SO_4/HNO_3, the working electrode (1 cm × 1 cm), Ag/AgCl in a (saturated KCL), and (3.0 MKC) as the reference electrode, and platinum foil as the counter electrode. The source of power for the degradation experiment was supplied by a 1 to 3 voltage range potentiometer capable of supplying current in the range of 1 to 15 mA. The source of light was obtained using a Sciencetech Inc Power Supply model 550 200 fitted with a liquid filter. A 10 cm distance was set between the reactor and the light sources to attain a light intensity of 0.27 W. The MB, BPA solutions (100 mL, 20 mg/L) and the sodium sulphate (0.1 M) as a supporting electrolyte were then introduced into the reactor system and then the electrodes were connected to the electrochemical instrument. During all degradation experiments, the dye solution was continuously stirred using a magnetic stirrer and all degradation experiments were performed for 2 h. Aliquots of the dyes were extracted at every 20 min interval and the concentrations of the dyes remaining in each extracted dye solution were determined using a PerkinElmer model Lambda 35 UV–Vis spectrophotometer. The percentage of degradation was calculated using Eq. 1, where C_o and C_t represent the initial concentration (mg/L) and the concentration at time interval t (mg/L).

$$Degradation(\%) = \frac{C_o - C_t}{C_o} \times 100 \quad (1)$$

3 Results and Discussion

3.1 XRD Analysis

Figure 1 shows the XRD patterns of PPy, Fe_3O_4, PPy/Fe_3O_4, and EG-PPy/Fe_3O_4. For the PPy XRD spectrum, no sharp peak was observed except for a broad peak located at 2θ = 24.4°, which is related to the short-range arrangement of the PPy chain [23]. For the Fe_3O_4 spectrum (Fig. 1b), peaks observed at 2θ = 18.5°, 30.2°, 35.5°, 43.2°, 53.3°, 57.2°, 62.7°, 71.1°, 74.1° and 75.1° indexed at 111, 220, 311, 400, 422, 511, 440, 442, 533 and 622 were crystalline planes of Fe_3O_4 nanoparticles with an inverse cubic spinel structure (JCPDS 19-0629) [24–27]. Figure 1c shows the XRD pattern of PPy/Fe_3O_4 composite with peaks associated with the amorphous polypyrrole and Fe_3O_4 observed. This shows that the amorphous polypyrrole exists on the Fe_3O_4 surface. The XRD pattern of EG is shown in Fig. 1d. A sharp diffraction peak observed at 2θ = 10°, 23°and55° which is indexed at 001, 002 and 004 was ascribed to the graphite intercalation compound of EG [28].

3.2 FTIR Analysis

The adsorption peaks of FTIR spectra of PPy, Fe_3O_4, EG and EG-PPy/Fe_3O_4 composite are depicted in Fig. 2. For Fe_3O_4 nanoparticles in Fig. 2a, the observed peak at 546 cm^{-1} was due to Fe–O band vibration. It is a characteristic peak for spinel structures for ferrite and occurs in this region due to stretching vibration band contributions relating to metals in the octahedral and tetrahedral sites of the oxide structure [29, 30]. The PPy spectra shown in Fig. 2b have characteristic peaks at 798, 922, 1042, 1199, 1288, 1475, 1564, and 1695 cm^{-1}. These were ascribed to C–H ring out-of-plane bending, C–C out-of-plane ring deformation, =C–H in-plane vibration, C–H stretching, C–N stretching vibration, pyrrole

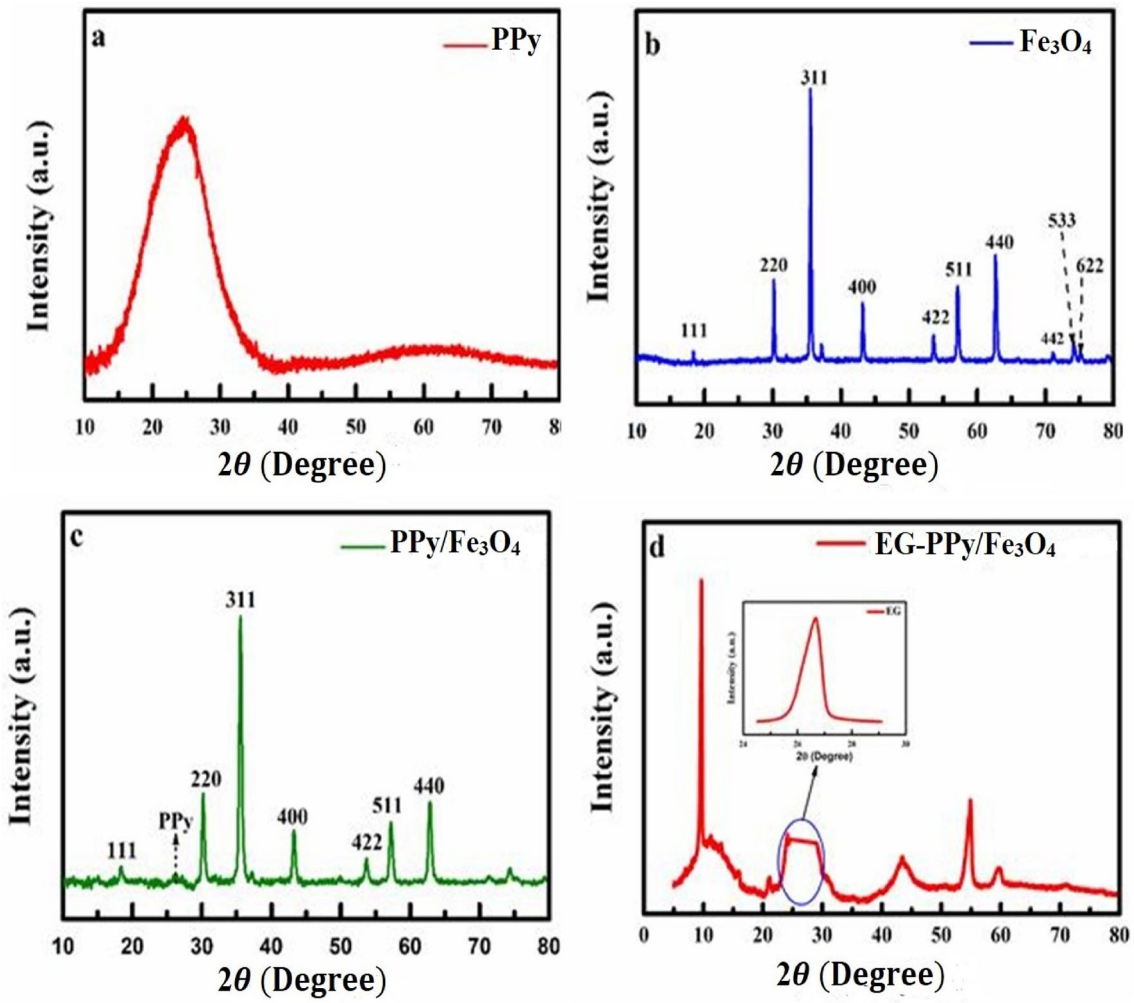

Fig. 1 XRD patterns of **a** PPy, **b** Fe_3O_4, **c** PPy/Fe_3O_4, and **d** EG-PPy/Fe_3O4

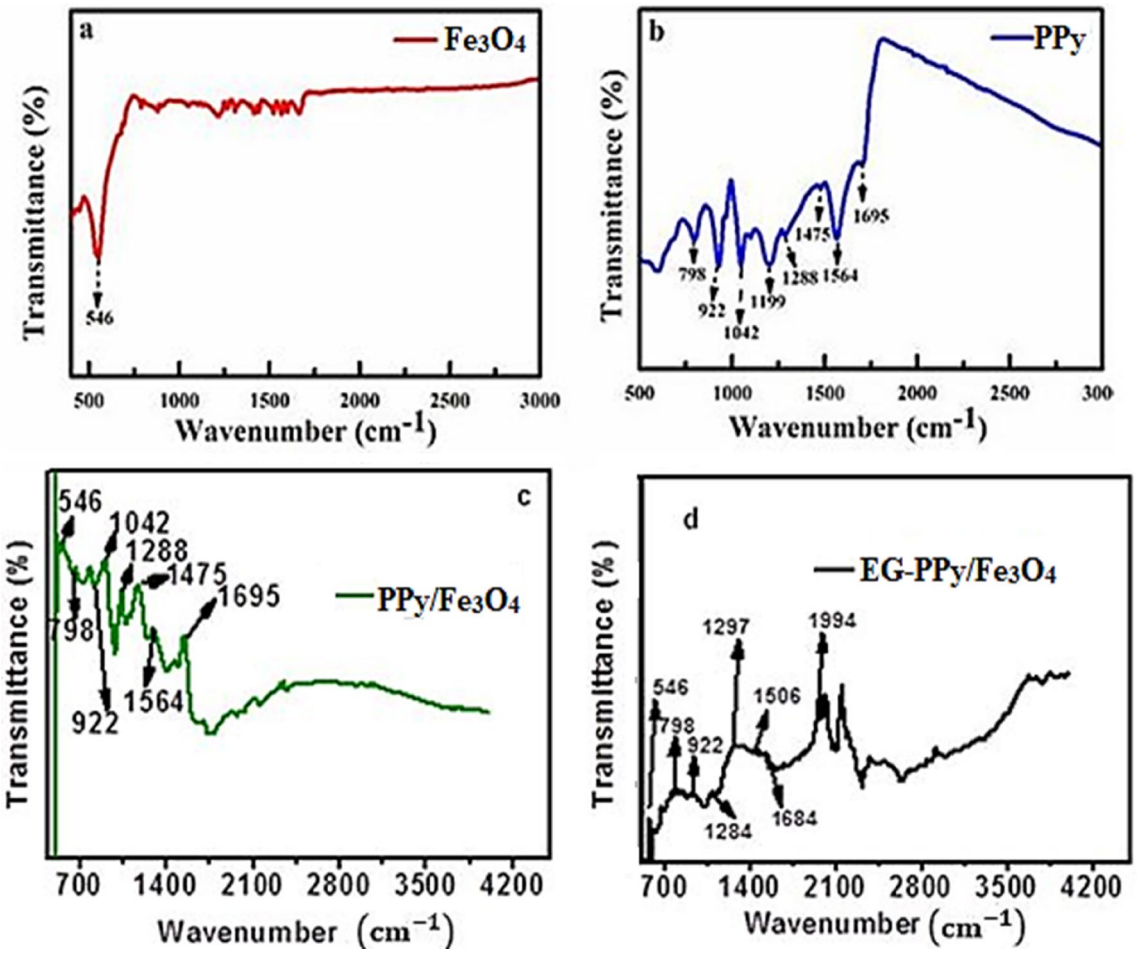

Fig. 2 FTIR spectra of **a** Fe_3O_4, **b** PPy, **c** PPy/Fe_3O_4 and **d** and EG-PPy/Fe_3O_4

ring stretching, conjugated C–N stretching and C–N in-plane bending vibration [25, 31–33]. The bands at 3450, 1684, and 1284 cm^{-1} in Fig. 2d were ascribed to the polymeric O–H stretching vibration of H_2O, stretching of the C=O bond of carboxylic groups and the stretching of C–OH of the COOH groups of EG [34].

3.3 SEM and EDS Analysis

Figure 3 shows the SEM images of Fe_3O_4, PPy/Fe_3O_4, EG-PPy/Fe_3O_4 and the EDX of EG-PPy/Fe_3O_4. The Fe_3O_4 is spherically shaped with smooth and uniform surface morphology (Fig. 3a). From Fig. 3b, the PPy was observed to encapsulate the Fe_3O_4 nanoparticle, which is fixed together in a partly or approximate spherical shape. A sizable flat layered aggregate structure (flask-like morphology) of EG-PPy/Fe_3O_4, which consists of multiple graphene sheets creating thick stacked layers was observed in Fig. 3c. The SEM image of the EG-PPy/Fe_3O_4 shows the successful decoration of PPy/Fe_3O_4 on the expanded graphite sheets. The EDX elemental analysis shown in Fig. 3d confirms the presence of C, O, and Fe elements, confirming the successful incorporation of the PPy/Fe_3O_4 into the EG layers. The element S was a result of the sulphuric acid used in treating the graphene flask during the synthesis process of the expanded graphene.

3.4 Brunauer–Emmett–Teller (BET) Analysis

The BET surface area analysis was aimed at determining the surface areas and pore volumes of the synthesized electrodes. Typically, catalysts possessing large surface areas and pore volumes display enhanced capacity to adsorb a variety of organic pollutants onto their surfaces, facilitating improved photoelectrochemical degradation of the pollutants. The results of the BET analysis of the EG, PPy/Fe_3O_4, and EG-PPy/Fe_3O_4 electrodes (Table 1) show that all the electrodes possess large surface areas, and pore volumes with EG-PPy/Fe_3O_4 exhibiting the highest surface area (18.86 $m^2\ g^{-1}$) and pore volume (0.07885 $cm^3\ g^{-1}$). All of the prepared electrodes are therefore expected to exhibit high pollutant degradation efficiencies, with EG- PPy/Fe_3O_4 potentially showing the highest efficiency.

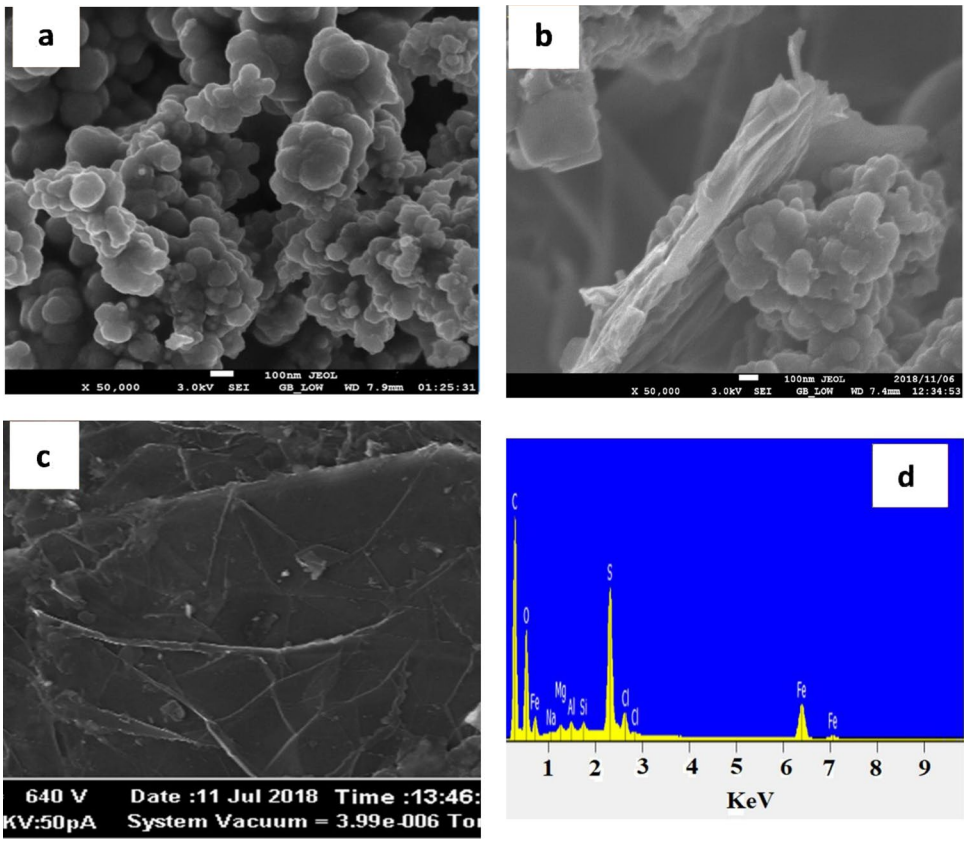

Fig. 3 SEM Image of **a** Fe_3O_4, **b** PPy/Fe_3O_4, **c** EG-PPy/Fe_3O_4 and **d** EDX of EG-PPy/Fe_3O_4

Table 1 BET surface area and pore volume for EG, Fe_30_4/PPy and EG@Fe_30_4/PPy

Sample	BET surface area ($m^2\ g^{-1}$)	Pore volume ($cm^3\ b^{-1}$)
EG	12.87	0.04589
Fe_30_4PPy	14.58	0.07678
EG/Fe_30_4PPy	18.86	0.07885

3.5 UV–Vis Analysis

The UV–Vis absorption spectra of the samples (Fig. 4) shows that the visible light absorptivity of Fe_3O_4 was enhanced by the introduction of PPy. Hence, the PPy/Fe_3O_4 demonstrated a higher visible light absorption ability than pure Fe_3O_4. A further increase in the visible light absorption of PPy/Fe_3O_4 occurred with the introduction of EG. Thus, the increased visible light activity of the EG-PPy/Fe_3O_4 electrode is caused by the synergistic effects of both PPy and EG. The EG behaved as a photosensitizer to improve the light absorption of the sample in the visible light region. High visible light activity implies enhanced pollutant degradation ability. The EG-PPy/Fe_3O_4 electrode, which exhibits the highest visible light activity, is expected, therefore, to

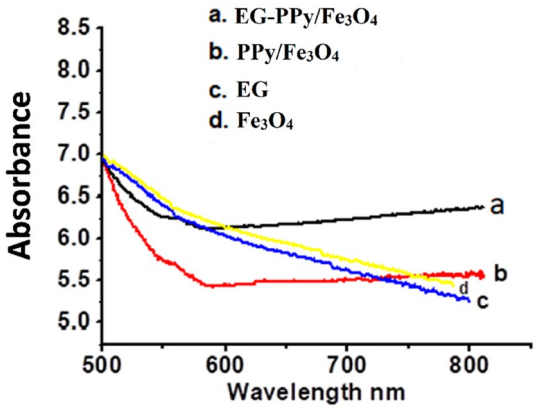

Fig. 4 UV–Vis absorbance spectra of (a) EG-PPy/Fe_3O_4, (b) PPy/Fe_3O_4, (c) EG and (d) Fe_3O_4

demonstrate the highest efficiency in the degradation of the pollutants. The absorption edge of PPy/Fe_3O_4 and EG-PPy/Fe_3O_4 was around 560 and 565 nm, respectively. The energy bandgap (E_g) was determined using the absorption spectra and it was calculated employing the Tauc relation in Eq. 2.

$$(\alpha hv)^2 = K(hv - E_g)^n \quad (2)$$

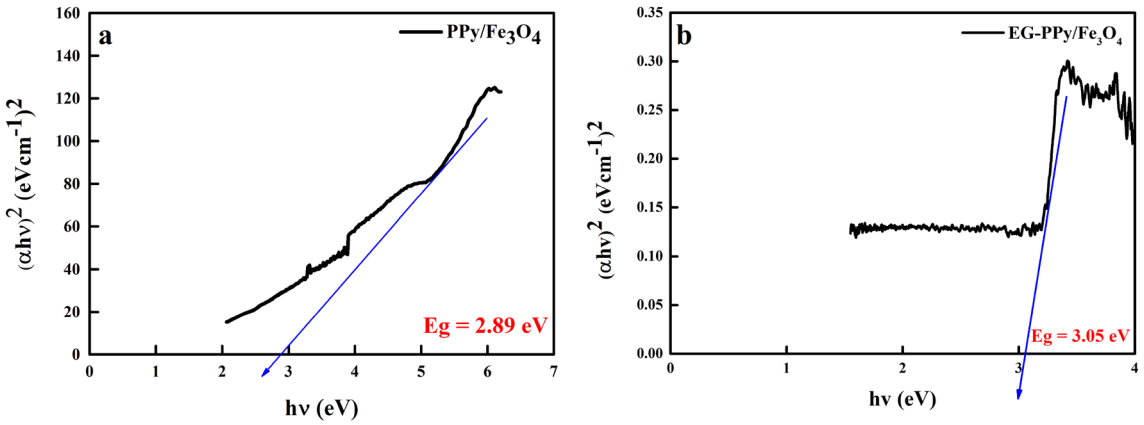

Fig. 5 Optical bandgaps of **a** PPy/Fe_3O_4 and **b** EG-PPy/Fe_3O_4

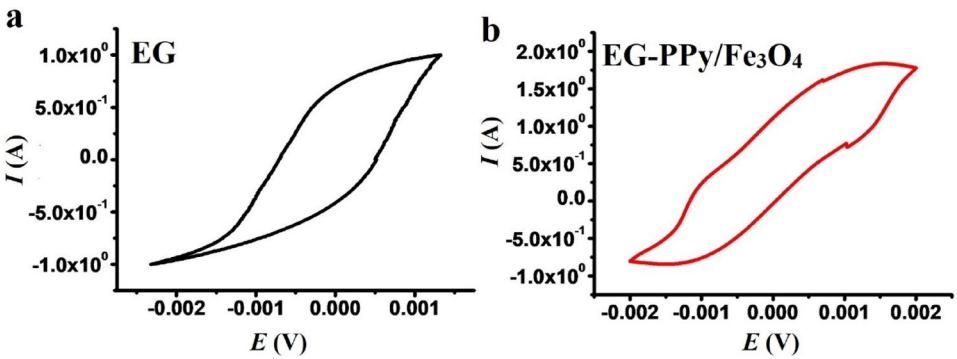

Fig. 6 Cyclic voltammetry (CV) of **a** EG and **b** EG-PPy/Fe_3O_4

where hv, K, α and n = 1 signify the photon energy, a constant, absorption coefficient and the direct bandgap. To estimate the optimal bandgap, a plot of $(\alpha hv)^2$ versus photon energy was employed. Figure 5a and b show the plots of $(\alpha hv)^2$ against hv for PPy/Fe_3O_4 and EG-PPy/Fe_3O_4, and the optical bandgap of PPy/Fe_3O_4 and EG-PPy/Fe_3O_4 was determined via the extrapolation of the straight line to the x-axis of the plots ($(\alpha hv)^2 = 0$). The estimated optical bandgap (E_g) was 2.89 and 3.05 eV for PPy/Fe_3O_4 and EG-PPy/Fe_3O_4, which were close to the results reported by Guo et al. [29] and Sadrolhosseini et al., (2016) [35].

3.6 Cyclic Voltammogram Analysis

The cyclic Voltammogram of EG and EG-PPy/Fe_3O_4 electrodes are shown in Fig. 6. The voltammogram was acquired using 10 mM potassium ferricyanide ([Fe (CN)6] − 3/ − 4) solution to probe the electrochemical potentials of the fabricated electrodes at 20 mV s^{-1}. Comparatively, the EG-PPy/Fe_3O_4 electrode (Fig. 6b) displayed a higher current than the EG electrode (Fig. 6a) as a result of the larger specific surface area of the EG-PPy/Fe_3O_4 caused by the presence of Fe_3O_4 nanoparticles in the composite.

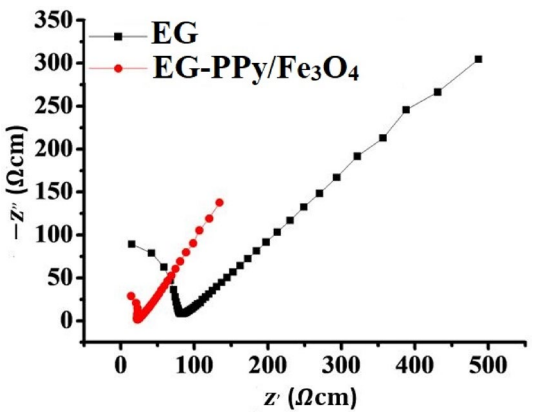

Fig. 7 Nyquist diagrams of EG and EG-PPy/Fe_3O_4 electrodes

3.7 Electrochemical Impedance Spectroscopy (EIS)

EIS is qualitative in the characterization of charge transfer resistance (R_{ct}) between photoanodes, and the organic dye being degraded from the wastewater. Figure 7 shows EIS measurements in terms of Nyquist diagrams on bare electrode EG and modified electrode EG- PPy/Fe_3O_4. A

relative view of real impedance (Z′ cm) and imaginary impedance (− Z″ cm), particularly at higher frequency show an arc radius of EG-PPy/Fe_3O_4 to be more compressed than that of EG. Based on the degradation efficiency criterion, the faster charge transfer resistance on EG-PPy/Fe_3O_4 makes it a potentially effective anode relative to EG photoanode.

3.8 Photoelectrochemical Degradation of BPA

UV measurements were carried out through a visible spectrophotometer, and the analyses from the EG-PPy/Fe_3O_4 photoelectrode are shown in Fig. 8a. From the analyses, it can be seen that degradation greatly occurs in the progression of time within the wavelength of 250 to 300 nm. Furthermore, the effectiveness of the degradation of BPA was carried out with three different photoelectrodes and techniques as shown in Figs. 8b and c, respectively. The degradation efficiency of BPA was monitored graphically in terms of time against degradation. In Fig. 8b, it can straightforwardly be seen that EG-PPy/Fe_3O_4 yields a better degradation efficiency. In terms of the techniques, the photoelectrochemical technique shows better degradation efficiency as can be seen in Fig. 8c.

3.9 Photoelectrochemical Degradation of Methylene Blue Dye

Figure 9 shows the degradation of MB under three different conditions. Firstly, the UV analysis was carried out to determine the efficiency of the EG-PPy/Fe_3O_4 photoelectrode in the degradation of MB. From 120 min of run shown in Fig. 9a, it can be seen that degradation progresses noticeably. In Fig. 9b, a relative utilization of three different photoelectrodes is displayed. Vividly, it can be seen that the EG-PPy/Fe_3O_4 electrode yields better degradation efficiency. The efficiencies of three different degradation techniques in the removal of MB from water were also assessed and the result is shown in Fig. 9c. It was realised that the photoelectrochemical technique led to higher degradation efficiency. Considering the analyses from the degradation of both MB and BPA, it can be seen that the photoelectrochemical technique and EG-PPy/Fe_3O_4 are the best technique and electrode respectively for effective degradation of these dyes in water.

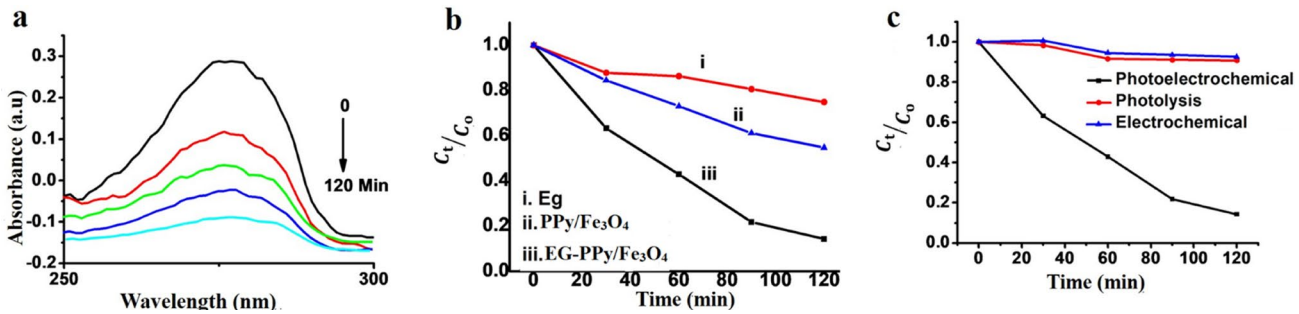

Fig. 8 **a** UV–Vis degradation profile of BPA dye in first 120 min by EG-PPy/Fe_3O_4 electrode, **b** BPA degradation efficiencies of (i) EG (ii) PPy/Fe_3O_4 (iii) EG-PPy/Fe_3O_4 and **c** Degradation profile of BPA on the bases of photolysis, electrochemical and photoelectrochemical degradations

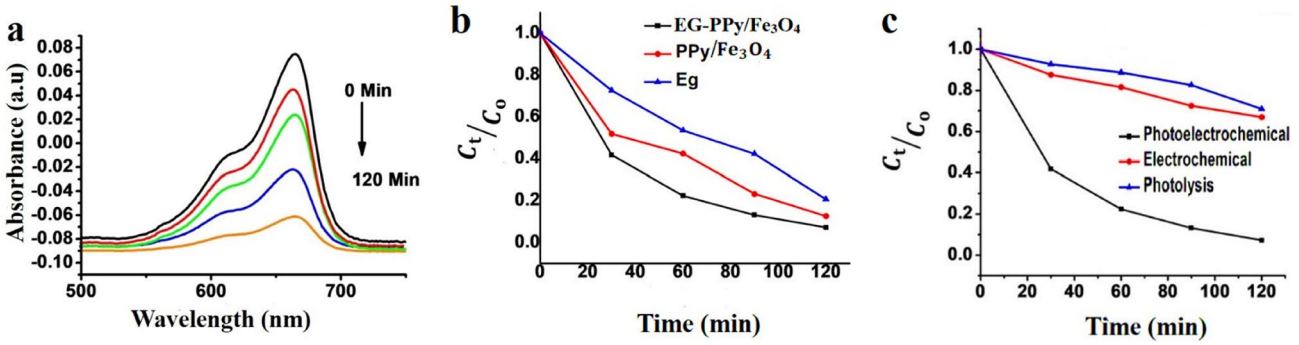

Fig. 9 **a** UV–Vis degradation profile of MB dye in first 120 min by EG-PPy/Fe_3O_4 electrode, **b** MB degradation efficiencies of EG, PPy/Fe_3O_4, and EG-PPy/Fe_3O_4, and **c** degradation profile of MB on the bases of photolysis electrochemical and photoelectrochemical degradations

4 Conclusions

The EG-PPy/Fe_3O_4 based electrode was synthesized and confirmed by the XRD and FTIR results. The electrodes were successfully applied to the degradation of BPA and MB with encouraging results. The EG-PPy/Fe_3O_4 composite exhibited higher visible light absorptivity compared to pure EG and PPy/Fe_3O_4. The EG-PPy/Fe_3O_4 was identified as the most effective electrode for the degradation of BPA and MB dyes. Also, compared to photolysis and photocatalytic degradation, the photoelectrochemical method resulted in significant degradation of BPA and MB using the EG-PPy/Fe_3O_4 electrode. The high efficiency of the EG-PPy/Fe_3O_4 electrode toward the degradation of the dyes is attributed to the synergistic effects of the individual components (PPy, Fe_3O_4 and EG) which enhanced the photocatalytic performance of the electrode by increasing its surface area and improving its visible light absorption. The photoelectrochemical degradation process resulted in improved degradation efficiency of 92% (MB) and 88% (BPA) within 240 min. The EG-PPy/Fe_3O_4 electrode is regarded as an effective electrode for the removal of BPA and MB from water. The data obtained from this study show that the EG-PPy/Fe_3O_4 nanocomposite can be used as an effective and functional nanoadsorbent for the sequestration/photodegradation of MB and BPA from water-soluble solutions. It is recommended that the EG-PPy/Fe_3O_4 electrode be tested for the treatment of real wastewater contaminated with textile and BPA waste.

Acknowledgements The authors wish to acknowledge the Faculty of Science/PDRF, Department of Chemical Sciences Centre for Nanomaterials Science Research and the University of Johannesburg, South Africa, for their financial support. We also acknowledge DST-CSIR and CENAM, Council for Scientific and Industrial Research, South Africa for making their instruments available for this research.

References

1. Garg A, Singhania T, Singh A, Sharma S, Rani S, Neogy A, Yadav SR, Sangal VK, Garg N (2019) Photocatalytic degradation of bisphenol-A using N, Co codoped TiO_2 catalyst under solar light. Sci Rep 9(1):765
2. Raizada P, Sudhaik A, Singh P (2019) Photocatalytic water decontamination using graphene and ZnO coupled photocatalysts: a review. Mater Sci Energy Technol 2:510–516
3. Mohapatra DP, Brar SK, Tyagi RD, Surampalli RY (2011) Occurrence of bisphenol A in wastewater and wastewater sludge of CUQ treatment plant. J Xenobiotics 1(1):e3–e3
4. Safabakhsh T, Pourzamani H (2016) Removal of bisphenol A from aqueous solutions using magnetic nanoparticles: investigation of adsorption isotherms. Int J Environ Health Eng 5(1):25
5. Li Q, Pan F, Li W, Li D, Xu H, Xia D, Li A (2018) Enhanced adsorption of bisphenol A from aqueous solution with 2-vinylpyridine functionalized magnetic nanoparticles. Polymers 10(10):1136
6. Orimolade BO, Adekola FA, Adebayo GB (2018) Adsorptive removal of bisphenol A using synthesized magnetite nanoparticles. Appl Water Sci 8(1):46
7. Abo R, Kummer NA, Merkel BJ (2016) Optimized photodegradation of bisphenol A in water using ZnO, TiO_2 and SnO_2 photocatalysts under UV radiation as a decontamination procedure. Drink Water Eng Sci 9(2):27–35
8. Zielińska M, Bułkowska K, Cydzik-Kwiatkowska A, Bernat K, Wojnowska-Baryła I (2016) Removal of bisphenol A (BPA) from biologically treated wastewater by microfiltration and nanofiltration. Int J Environ Sci Technol 13(9):2239–2248
9. Dinçer AR, Güneş Y, Hanci TÖ, Güneş E, Khoei S (2018) Effects of endocrine-disrupting compounds (bisphenol A and octhyl phenol ethoxylate) on COD removal efficiency. SAR J 1(2):35–41
10. Hassan MM, Carr CM (2018) A critical review on recent advancements of the removal of reactive dyes from dyehouse effluent by ion-exchange adsorbents. Chemosphere 209:201–219
11. Aquino JM, Rocha-Filho RC, Ruotolo LA, Bocchi N, Biaggio SR (2014) Electrochemical degradation of a real textile wastewater using β-PbO2 and DSA® anodes. Chem Eng J 251:138–145
12. Khatri J, Nidheesh PV, Singh TA, Kumar MS (2018) Advanced oxidation processes based on zero-valent aluminium for treating textile wastewater. Chem Eng J 348:67–73
13. Sandhya S (2010) Biodegradation of azo dyes under anaerobic condition: role of azoreductase. Biodegradation of azo dyes. Springer, Berlin, Heidelberg, pp 39–57
14. Sudarni DHA, Aigbe UO, Ukhurebor KE, Onyancha RB, Kusuma HS, Darmokoesoemo H et al (2021) Malachite green removal by activated potassium hydroxide clove leaf agrowaste biosorbent: characterization, kinetic, isotherm, and thermodynamic studies. Adsorpt Sci Technol. https://doi.org/10.1155/2021/1145312
15. Torres RA, Pétrier C, Combet E, Carrier M, Pulgarin C (2008) Ultrasonic cavitation applied to the treatment of bisphenol A. Effect of sonochemical parameters and analysis of BPA by-products. Ultrason Sonochem 15(4):605–611
16. Ama OM, Khoele K, Anku WW, Ray SS (2019) Photoelectrochemical degradation of 4-nitrophenol using CuO-ZnO/exfoliated graphite nanocomposite electrode. Int J Electrochem Sci 14(3):2893–2905
17. Singh P, Shandilya P, Raizada P, Sudhaik A, Rahmani-Sani A, Hosseini-Bandegharaei A (2018) Review on various strategies for enhancing the photocatalytic activity of graphene based nanocomposites for water purification. Arab J Chem 13(1):3498–3520
18. Arsac F, Bianchi D, Chovelon JM, Conchon P, Ferronato C, Lair A, Sleiman M (2008) Photocatalytic degradation of organic pollutants in water and in air. An analytical approach. Mater Sci Eng C 28(5–6):722–725
19. Jung KW, Lee SY, Lee YJ, Choi JW (2019) Ultrasound-assisted heterogeneous Fenton-like process for bisphenol A removal at neutral pH using hierarchically structured manganese dioxide/biochar nanocomposites as catalysts. Ultrason Sonochem 57:22–28
20. Yu F, Bai X, Yang C, Xu L, Ma J (2019) Reduced graphene oxide–P25 nanocomposites as efficient photocatalysts for degradation of bisphenol A in water. Catalysts 9(7):607
21. Neamtu M, Nadejde C, Hodoroaba VD, Schneider RJ, Verestiuc L, Panne U (2018) Functionalized magnetic nanoparticles: synthesis, characterization, catalytic application and assessment of toxicity. Sci Rep 8(1):1–1
22. Rasheed T, Bilal M, Nabeel F, Adeel M, Iqbal HM (2019) Environmentally-related contaminants of high concern: potential sources and analytical modalities for detection, quantification, and treatment. Environ Int 122:52–66
23. Tarmizi EZM, Baqiah H, Talib ZA, Kamari HM (2018) Preparation and physical properties of polypyrrole/zeolite composites. Res Phys 11:793–800

24. Bai L, Li Z, Zhang Y, Wang T, Lu R, Zhou W, Gao H, Zhang S (2015) Synthesis of water-dispersible graphene-modified magnetic polypyrrole nanocomposite and its ability to efficiently adsorb methylene blue from aqueous solution. Chem Eng J 279:757–766
25. Li Y, Chen G, Li Q, Qiu G, Liu X (2011) Facile synthesis, magnetic and microwave absorption properties of Fe_3O_4/polypyrrole core/shell nanocomposite. J Alloys Compd 509(10):4104–4107
26. Li N, Tian Y, Zhao J, Zhan W, Du J, Kong L, Zhang J, Zuo W (2018) Ultrafast selective capture of phosphorus from sewage by 3D Fe_3O_4@ZnO via weak magnetic field enhanced adsorption. Chem Eng J 341:289–297
27. Shanehsaz M, Seidi S, Ghorbani Y, Shoja SM, Rouhani S (2015) Polypyrrole-coated magnetic nanoparticles as an efficient adsorbent for RB19 synthetic textile dye: removal and kinetic study. Spectrochim Acta A 149:481–486
28. Siburian R, Sihotang H, Raja SL, Supeno M, Simanjuntak C (2018) New route to synthesize of graphene nano sheets. Orient J Chem 34(1):182
29. Guo J, Gu H, Wei H, Zhang Q, Haldolaarachchige N, Li Y, Young DP, Wei S, Guo Z (2013) Magnetite–polypyrrole metacomposites: dielectric properties and magnetoresistance behavior. J Phys Chem C 117(19):10191–10202
30. Lopez JA, González F, Bonilla FA, Zambrano G, Gómez ME (2010) Synthesis and characterization of Fe_3O_4 magnetic nanofluid. Revista Latinoamericana de Metalurgia y Materiales 30(1):60–66
31. Bhaumik M, Maity A, Srinivasu VV, Onyango (2011) Enhanced removal of Cr(VI) from aqueous solution using polypyrrole/Fe_3O_4 magnetic nanocomposite. J Hazard Mater 190:381–390
32. Deng J, Peng Y, He C, Long X, Li P, Chan AS (2003) Magnetic and conduction Fe_3O_4-polypyrrole nanoparticles with core-shell structure. Polym Int 52(7):1182–1187
33. Sidhu GK, Kumar R (2018). Study the structural and optical behaviour of conducting polymer based nanocomposites: ZrO_2-polypyrrole nanocomposites. In: IOP conference series: materials science and engineering 360(1):012038. IOP Publishing
34. Nezhad AA, Alimoradi M, Ramezani M (2018) One-step preparation of graphene oxide/polypyrrole magnetic nanocomposite and its application in the removal of methylene blue dye from aqueous solution. Mater Res Express 5(2):025508
35. Sadrolhosseini AR, Abdul Rashid S, Noor ASM, Kharazmi A, Lim HN, Mahdi M (2016) Optical band gap and thermal diffusivity of polypyrrole-nanoparticles decorated reduced graphene oxide nanocomposite layer. J Nanomater 2016:1–8